

On the Origin of Room-Temperature Amplified Spontaneous Emission in CsPbBr₃ Single Crystals

Donggyu Kim, Hongsun Ryu, Soo Yeon Lim, Kyle M. McCall, Jongwoo Park, Sungdo Kim, Tae Jung Kim, Jeongyong Kim, Yong Soo Kim, Mercouri G. Kanatzidis, Hyeonsik Cheong, and Joon I. Jang*

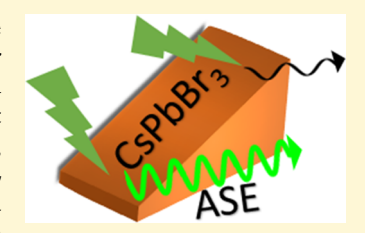
ACCESS

Metrics & More

Article Recommendations

Supporting Information

ABSTRACT: CsPbBr₃ is an all-inorganic halide perovskite with excellent photoluminescence (PL) properties for laser applications. Amplified spontaneous emission (ASE) is a prerequisite for lasing and typically observed from low-dimensional CsPbBr₃ nanostructures, where quantum confinement enhances ASE. However, a gain medium for lasing should be prepared into a robust bulk form that works under intense light illumination. Here, we demonstrate that bulk CsPbBr₃ single crystals exhibit highly efficient ASE with a threshold of 46 MWcm⁻² at 520 nm, if PL reabsorption via the indirect Rashba gap is properly suppressed by thickness control. Based on a series of spectroscopic and microscopic measurements, we show that this below-the-gap



absorption can significantly alter the PL feature and even the apparent color of the crystal depending on the crystal size. Our results show that a thin CsPbBr₃ single crystal can be utilized for lasing applications when engineered into a submillimeter thickness for effective light—matter interaction.

■ INTRODUCTION

Halide perovskites are emerging photovoltaic and optoelectronic materials with the ongoing upsurge of recent research followed by successful applications to solar cells and lightemitting diodes (LEDs). They possess excellent optical behaviors such as a large absorption coefficient, a long carrier lifetime, a long diffusion length, and cost-effective preparation. 9-12 In addition to these properties, amplified spontaneous emission (ASE) and lasing at low thresholds have been observed from both all-inorganic and organic-inorganic halide perovskites at room temperature. 13-17 Also, the band gap of halide perovskites can be easily tuned in the visible regime by adjusting their halide composition, 18,19 showing their potential as a new optical gain medium for visible lasers. A high optical gain has been recorded in various forms of halide perovskites including thin films, ^{20,21} micro-/nanocrystals, ^{19,22–25} quantum dots, ^{26,27} and other structures. ^{15,16,28} Moreover, different types of perovskite-based lasers such as microcavity lasers, ²⁹ distributed feedback lasers, ^{30,31} whispering gallery mode lasers, ^{32,33} and random lasers have been demonstrated. For more practical and immediate applications, a bulk single crystalline form is required for the design of solid-state lasers, together with its robust nature under intense optical pumping. However, ASE in bulk single crystals is significant only at low temperatures.³⁴ Recently, two-photon-induced ASE was achieved in a bulk single crystal at room temperature, but this nonlinear optical excitation requires very a high input intensity of 18 GWcm⁻², which is more than 100 times bigger than the ASE threshold of the perovskites in other forms.³ fact, room-temperature ASE has not been realized in any

perovskite single crystal under ordinary one-photon absorption. Therefore, the origin of ASE in single crystals is relatively unexplored compared to ASE from perovskite nanostructures, in which various mechanisms involving carriers, ^{29,36} excitons, ^{37–39} polaritons, ^{40–42} trions, ⁴³ and biexcitons ^{44,45} induce efficient ASE under quantum confinement. But quantum confinement is not applicable in macroscopic single crystals at room temperature.

To understand and even realize room-temperature ASE, we carefully investigated position-dependent photoluminescence (PL) response from high-quality CsPbBr₃ single crystals as a function of both excitation intensity (I) and wavelength (λ) as well. Under low excitation levels, our crystals exhibit identical PL response at room temperature independent of the excitation position. As the excitation level increases, however, ASE becomes active at particular spots in the crystals, which are rather sporadically distributed over the entire specimens but more frequently encountered near the edge of the crystals. The corresponding threshold intensity for ASE at λ = 520 nm was found to be about 46 MWcm⁻². To examine the ASE-active regions more closely, we employed micro-PL and micro-Raman spectroscopy, together with microscope imaging. Most of the crystal area appears dark gray under an optical



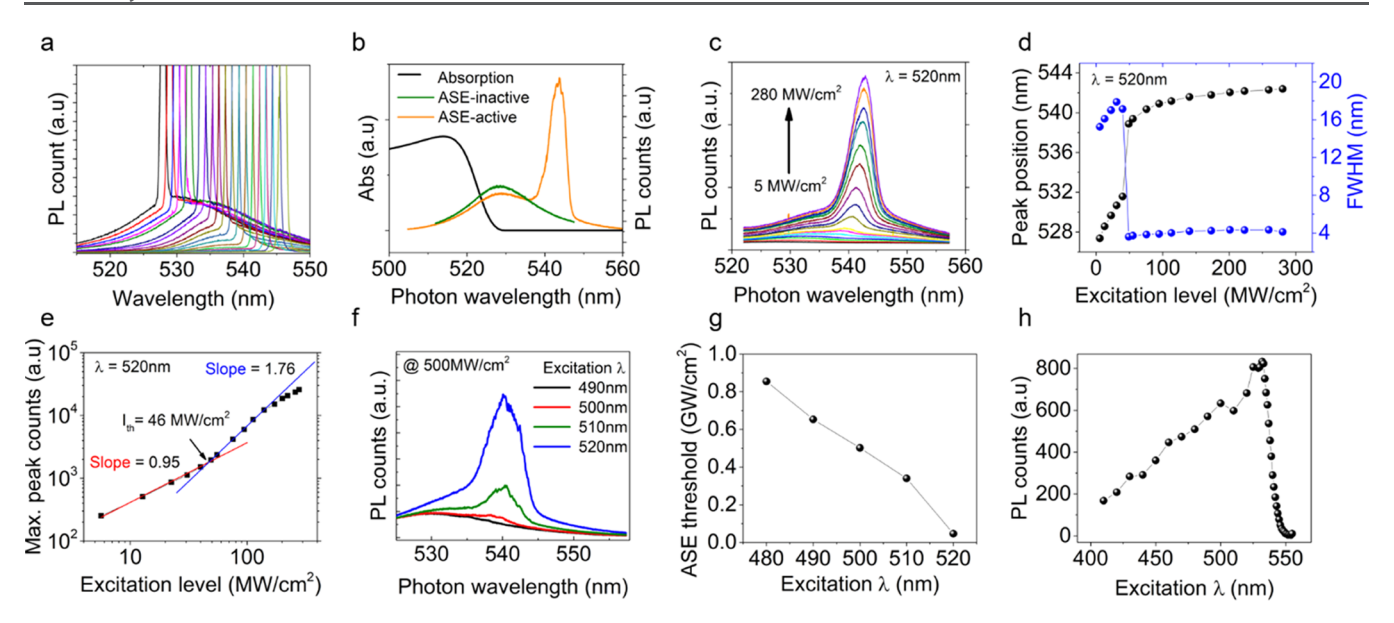


Figure 1. (a) PLE spectra from CsPbBr₃ at room temperature when λ was tuned from 548 nm to 528 nm, showing that CsPbBr₃ yields measurable PL even under below-the-gap excitation. This unusual behavior is attributed to indirect optical transition across the Rashba gap. Each sharp peak on top of the PL spectrum corresponds to the scattered laser light. (b) Typical room-temperature PL spectra at λ = 500 nm obtained from ASE-active (orange) and ASE-inactive (green) regions under the same excitation condition. The black trace corresponds to the absorption spectrum, whose absorption edge is consistent with the PL peak. (c) Evolution of the PL spectra at λ = 520 nm as I was varied from 5 to 280 MWcm⁻². (d) Peak position (black) and FWHM (blue) of the PL as a function of I. (e) Log-log plot of the PL counts as a function of I. A clear threshold behavior is observed for ASE, where the power exponents for the red and blue lines are indicated, respectively. (f) PL spectra at λ = 490 nm (black), 500 nm (red), 510 nm (green), and 520 nm (blue), respectively, showing a clear λ dependence in the ASE threshold. (g) ASE threshold vs λ . (h) PL counts vs λ at slightly below the ASE threshold.

microscope, and these regions are ASE-inactive. In contrast, ASE-active regions appear bright orange in color and show distinct PL responses at both room and low temperatures. However, micro-Raman signals from these two regions turned out to be identical, with no evidence of other phases like CsPb₂Br₅ and Cs₄PbBr₆ embedded as microcrystallites. Upon close examination of the ASE-active spots under the microscope, we found that they are distributed near small cracks developed over the surface and edge of the crystal. This indicates that these ASE-active spots are isolated from the bulk, thereby undergoing different levels of optical absorption, which, in turn, affect the apparent color and the PL spectra. To confirm this, we ground gray-colored crystals and confirmed that they indeed become bright orange in color and exhibit ASE. Ultimately, we confirmed persistent ASE from a bulk single crystal when its thickness is reduced to the submillimeter level, thereby minimizing the energy loss by reabsorption. While most of the gain materials require a large thickness, which can be several centimeters, CsPbBr3 single crystals can be utilized as an efficient gain medium with a much thinner thickness for energy- and cost-effective laser applications.

■ EXPERIMENTAL SECTION

Preparation of CsPbBr₃ **Single Crystals.** Our CsPbBr₃ single crystal was synthesized by the Bridgman method. First, 27.32 g (100 mmol) of PbO was dissolved in 100 mL of 48% aqueous HBr to produce a pale solution. PbBr₂ prepared according to the procedure described in the reference ⁴⁶ and 8.512 g (40 mmol) of CsBr (Sigma-Aldrich, SN) were thoroughly mixed and flame-sealed in a quartz ampule (13 mm o.d.) under vacuum (2×10^{-3} mbar) and reacted in a box furnace at 650 °C. The resulting ingot was powdered and sealed in a fresh quartz ampule with a sharp tip for Bridgman crystal growth. The single crystalline ingot was grown in a two-zone Bridgman furnace with the hot and cold zones at 800 and 400 °C, respectively. A

translation speed of 2 mm per hour was used for the growth, and an orange transparent ingot was obtained (1 cm in diameter). The asgrown $CsPbBr_3$ ingots were cut into wafers perpendicular to the growth direction using an Accutom-50 diamond-bladed saw. The resulting wafers were polished to optical quality using silicon carbide sandpaper with successively smaller particle sizes down to 2 μm (12 000 grit). The final wafers were etched in HBr for 30 s and rinsed in toluene to remove debris. The final wafer was cut into a rectangular shape for actual use in the experiments.

 $\ddot{\text{X}}$ -ray Diffraction (XRD). $\ddot{\text{X}}$ -ray diffraction (XRD) of our CsPbBr₃ single crystal was measured with a Rigaku Miniflex600 diffractometer (CuK α , operating at 15 mV and 40 kV) by centering the crystal in the sample holder, with the polished surface of the crystal facing the beam.

Ellipsometry. The absorption coefficient of our single crystal was determined at room temperature by spectroscopic ellipsometry using an M2000FI (J. A. Woollam Co). The ratio between the amplitude and the phase difference of the complex reflectances for s and p polarized light was measured and the refractive index n and the extinction coefficient k were determined through multilayer calculation. The absorption coefficient (α) can be calculated from k using a relation $\alpha(\lambda) = 4\pi k/\lambda$.

PL and PLE Experiments. Our samples were mounted directly to the cold finger of a cryostat (JANIS CCS-150) for temperature-dependent optical measurements. Our PL and PLE experiments including all ASE measurements were performed using a pulsed laser. An Nd:YAG laser (EKSPLA PL 2250) with a 50 Hz repetition rate and a 30 ps pulse width was used as a pump source for the remaining passive laser systems for wavelength tuning. A 1064 nm beam was frequency tripled to 355 nm through a Harmonic Unit (EKSPLA H400), which pumped an optical parametric oscillator (EKSPLA PG403) that produced twin photons in terms of the signal (410–709 nm) beam and the idler (710–2300 nm) beam. A proper excitation wavelength was selected for the PL and PLE measurements and the input laser beam was focused onto the sample with a beam diameter of 100 μ m. The reflection geometry was used for the collection of the PL to minimize the effect of reabsorption over the macroscopic

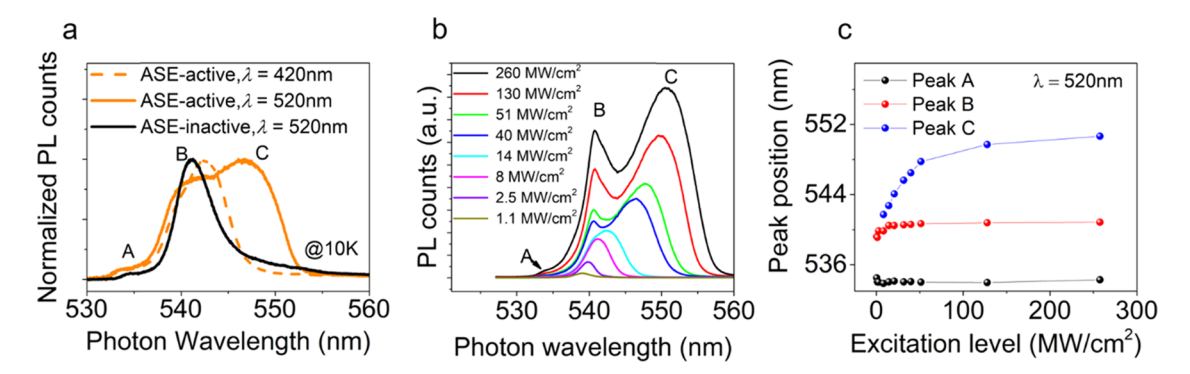


Figure 2. (a) Normalized PL spectra at 10 K from an ASE-inactive site at $\lambda = 520$ nm (black) and from an ASE-active site at $\lambda = 420$ nm (dashed orange) and 520 nm (orange), respectively, at I = 70 MWcm⁻² (A: exciton, B: P-band, and C: ASE). (b) Evolution of the PL spectra at $\lambda = 520$ nm from the ASE-active site at 10 K, where I was varied from 1.1 to 260 MWcm⁻². (c) PL peak position vs I. The C peak exhibits a significant red shift with increasing I.

sample thickness (3 mm) that significantly alters the PL when collecting using the transmission geometry. The collected PL via a fiber-optic bundle was dispersed using a Horiba iHR320 spectrometer and detected by a charge-coupled device (CCD) camera. The contribution from the scattered laser light was minimized using a polarizer with a cross polarization setup.

Micro-PL and Micro-Raman Spectroscopy and Microscopy. Micro-Raman and micro-PL measurements were conducted using a diode-pumped solid-state (DPSS) laser with a wavelength of 514.4 nm (2.41 eV), an Ar+ laser with a wavelength of 514.5 nm (2.41 eV), a He–Cd laser with a wavelength of 441.6 nm (2.81 eV), and a He–Ne laser with a wavelength of 632.8 nm (1.96 eV). A $50 \times$ (N.A. = 0.8) and a $40 \times$ (N.A. = 0.6) objective lens was used to focus the laser to a spot of $\sim 1~\mu m$ diameter with a power of $100~\mu W$. The light from the crystal was dispersed using a Jobin–Yvon Horiba iHR550 spectrometer (2400 and 1200 grooves/mm). A CCD using liquid nitrogen for cooling was used to detect the signal. To access the low-frequency range down to 5 cm⁻¹, reflective volume Bragg gratings (OptiGrate) were used as notch filters to remove the Rayleigh scattered signal. Low-temperature Raman measurements at 77 K were carried out in vacuum using an optical cryostat (Oxford Micorostat He2).

■ RESULTS AND DISCUSSION

Our bulk CsPbBr3 single crystal was synthesized by the Bridgeman technique. 46 The crystal was cut and polished into several 3-mm-thick samples with a rectangular shape. For basic characterization of the samples, the X-ray diffraction (XRD) pattern, the PL, and the absorption spectra were measured at room temperature. The XRD pattern of our CsPbBr3 indicates that the sample is oriented along the (001) direction (Figure S1). We conducted PL excitation (PLE) spectroscopy by varying λ from 550 nm to 528 nm (keeping $I = 100 \text{ MWcm}^{-2}$) to identify both the direct fundamental gap and the indirect Rashba gap (Figure 1a). Although the main absorption edge is around 528 nm, as confirmed by both PL (green) and absorption (black) spectra in Figure 1b, actual absorption starts from 548 nm, which corresponds to indirect transition involving phonon scattering. This below-the-gap absorption in bulk perovskites of a millimeter thickness is typical and well established in the literature.⁴⁷ The PL increases and blue-shifts as λ was varied toward the band-edge wavelength of 528 nm, where the sharp peak on top of each PL spectrum arises from the scattered laser light. The location of the PL peak is plotted as a function of λ in Figure S2a. The corresponding PL counts are also plotted in Figure S2b, in which the variation in the PL counts clearly indicates the presence of an indirect transition slightly below the direct gap as a consequence of the dynamic

Rashba effect. 48,49 Interestingly, during the PLE experiments, ASE was observed from specific positions on the sample surface. The orange trace in Figure 1b corresponds to a typical PL spectrum exhibiting ASE at the high-wavelength side of the main PL. Most of the sample surface was found to be ASE-inactive, with the ASE-active sites being sporadically distributed on the sample surface and more concentrated near the crystal edge. We found that one specimen does not show any ASE when we scanned the entire area of the crystal. This implies that ASE is inactive in bulk single crystals, and therefore, the ASE-active regions seem to occur due to unknown extrinsic effects.

We first characterized the properties of ASE at room temperature. Figure 1c shows the evolution of the PL spectra at $\lambda=520$ nm as I was increased from 5 to 280 MWcm⁻² (Figure S3a for the threshold behavior near the ASE onset). The corresponding peak position and the full-width at half-maximum (FWHM) are shown in Figure 1d. Below the ASE threshold, the PL spectra from ASE-active and ASE-inactive regions are identical. We confirmed that the ASE-inactive PL does not undergo any shape change with increasing excitation level within our experimental range. In contrast, the ASE-active region shows the onset of the ASE peak near 538 nm at I=46 MWcm⁻². Note that there is a sharp drop in the FWHM above the threshold, which is typical of ASE. The observed red shift of the ASE peak with further increasing I arises from band-gap renormalization. S0

The ASE threshold is further confirmed with emission counts vs I plotted on a logarithmic—logarithmic (log—log) scale (Figure 1e, see also Figure S3b for the linear—linear scale), where the slope of the fit indicates the power exponent k in the relation between the PL counts and I (PL $\propto I^k$). Below the threshold, the PL counts increase with a power exponent k=0.95, which arises from radiative recombination of free carriers in the quasi-steady state (k=1). However, above the threshold, the k value suddenly changes to 1.76, indicating amplified emission of the PL. The noticeable deviation from the fit at very high excitation levels can be attributed to density-dependent nonradiative Auger decay.

The ASE threshold shows a strong dependence on λ for every ASE-active spot. For example, a striking difference in the PL spectra is observed in Figure 1f, where the same ASE-active spot was excited at 490 nm (black), 500 nm (red), 510 nm (green), and 520 nm (blue), respectively, under the same $I = 500 \text{ MWcm}^{-2}$. No ASE was observed at $\lambda = 490 \text{ nm}$, ASE

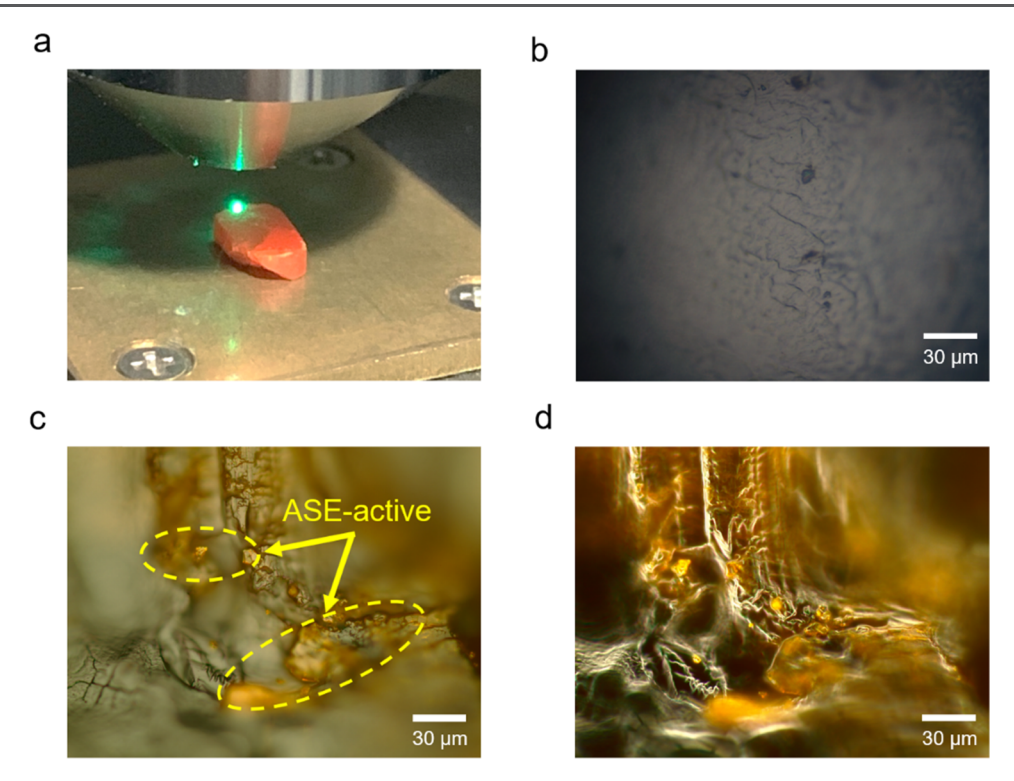


Figure 3. (a) Representative photograph of our CsPbBr₃ single crystal under cw laser illumination (micro-PL setup). (b) Microscopy image taken at the center of the single crystal. (c) Bright-field microscopy image and (d) dark-field microscopy image of the sample surface near the edge, showing several ASE-active regions (bright orange in color). ASE predominantly occurs in the orange-colored area.

appears at $\lambda = 500-520$ nm, and ASE is most significant at $\lambda =$ 520 nm. In fact, we confirmed that the minimum ASE threshold was obtained at 520 nm. The threshold value increases with decreasing λ and there is no ASE when λ is below 480 nm (Figure 1g). The observed wavelength dependence can be explained by Auger effects, leading to a carrier density drop and heating, where the latter arises from band-gap energy transfer as a consequence of nonradiative recombination of carriers.⁵³ This is more pronounced for carriers having a higher gas temperature.⁵⁴ Incident photons that have a higher energy than the band gap initially generate hot carriers by converting their excess energy to the kinetic energy of carriers, which is directly proportional to the gas temperature. Our claim is supported by Figure 1h that shows a significant drop in the PL counts when λ is decreased. This prevents efficient population inversion near the light cone, which is a prerequisite for ASE. This tendency results in the higher ASE threshold for the shorter excitation wavelength.

We carried out low-temperature PL spectroscopy to further understand the ASE behavior. The evolution of the PL spectra from room temperature to 10 K is shown in Figure S4. Figure 2a illustrates normalized PL spectra at 10 K observed from an ASE-inactive point (black) and an ASE-active point (orange) at $\lambda = 520$ nm and at I = 70 MWcm⁻². At this low temperature, the ASE-active PL is essentially excitonic and consists of three peaks at 534 nm (A), 541 nm (B), and 547 nm (C) at $I \ge 15$ MWcm⁻². The A and B peaks were observed everywhere on the single crystal and arise from radiative recombination of excitons and so-called P-band emission, respectively. The latter is caused by radiative recombination of photon-like excitons (polaritons) near the polariton bottleneck after inelastic exciton—exciton scattering. On the other hand, the C peak was mainly observed at the ASE-active sites. Figure 2b shows

the evolution of the ASE-active PL spectra with increasing I from 1.1 to 260 MWcm⁻² at $\lambda = 520$ nm. With I up to 14 MWcm⁻², P-band emission is dominant due to enhanced probabilities for inelastic exciton-exciton scattering. We found that P-band emission was observed only below 70 K (Figure S4). This implies that the Saha transition between free carriers and excitons occurs at 70 K since P-band emission involves scattering between excitons. Upon further increase in I, the C peak emerges and steeply increases to dominate the PL response. While the peak shift for both A and B peaks are negligible and minor, respectively, the C peak red-shifts severely and broadens with increasing excitation power (Figure 2c). These spectral signatures are typical of Mott transition, ⁵¹ leading to the formation of electron-hole plasma (EHP); also see Figure S5 for the *I* dependence at 80 K.⁵⁵A minor red shift in P-band emission arises from polaritons generated deeper inside the bottleneck due to enhanced exciton-exciton scattering. Here, we emphasize that our time-integrated PL spectra capture both B and C peaks at the same time. In fact, the C peak is dominant just after the laser pulse. As the carrier density drops with time, however, the C peak gradually transforms into the B peak, which is accompanied by Mott transition from the metallic plasma to the insulating excitonic phase.⁵⁶ Note that the C peak is absent when the ASE-active site was excited at 420 nm (dashed orange), as shown in Figure 2a. Figure S4 also confirms that the C peak evolves into the ASE peak with increasing temperature.

The most peculiar behavior of ASE in CsPbBr₃ single crystals is its strong position dependence. To resolve this critical issue, the micro-PL response was measured using a continuous wave (cw) laser (Figure 3a). Although the apparent color of our single crystal is pale orange, we found that the crystal surface looks dark gray when observed under a confocal

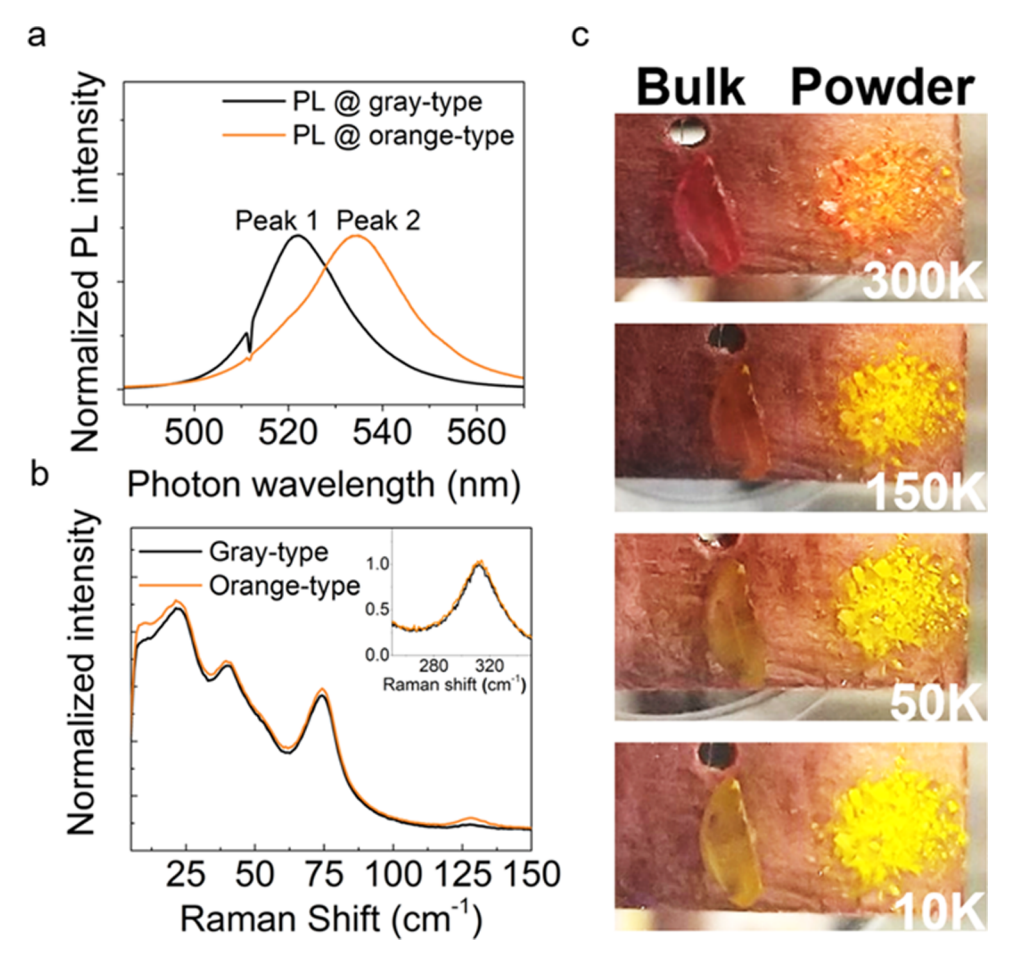


Figure 4. (a) Normalized micro-PL spectra at room temperature obtained from the gray area (black) and the orange area (orange), respectively, under cw illumination (λ = 514.4 nm). The dip feature near 514.4 nm arises from the Raman filter. (b) Low-frequency Raman spectra at λ = 632.8 nm obtained from the gray region (black) and the orange region (orange), respectively. Both spectra are normalized at the peak at 312 cm⁻¹. Inset: the second-order phonon mode of [PbBr₆]⁴⁻. (c) Apparent color change of the bulk CsPbBr₃ crystal and ground powders at several temperatures from 300 to 10 K. Clearly, reabsorption depends both on temperature and crystal size.

microscope (Figure 3b). This is a function of a confocal microscope, and the gray color results from the loss of scattered light into the bulk of the crystal and a lack of reflected light from the back surface. Intriguingly, however, microscopy images taken over the crystal surface revealed the existence of small spots in a bright orange color, which are randomly and scarcely distributed over the sample surface with higher occurrence near the crystal edge. For example, Figure 3c shows such orange spots near one edge of the crystal (see Figure S6 for more examples). Such spots are the result of reflection near the confocal plane of the microscope, and indicate that there are distinct microcrystals with loose or cracked surfaces. To confirm that this color difference does not arise from any other external light source, we also took the dark-field image (Figure 3d), which shows an even clearer color contrast between dark gray and bright orange. From the dark-field image, we confirmed that the orange spots are indeed orange in color and much brighter than the gray area, indicating that more scattered light is present from the orange spots under white light illumination. We found that each ASEactive point precisely coincides with the position for microcrystalline orange areas, confirming that ASE arises only at orange-type regions and explaining its strong position dependence. To check any difference in the PL response, we measured the PL from the gray and the orange areas using the

DPSS laser ($\lambda = 514.4$ nm). Interestingly, with the cw beam tightly focused onto the specimen (1 μ m in diameter), the PL spectra from the dark gray and bright orange regions are indeed different, as shown by the black and the orange traces in Figure 4a. At first glance, the PL spectra seem different in that their maximum positions are 522 nm (peak 1) and 534 nm (peak 2). While scanning various excitation spots over the sample, we found that the relative PL brightness between peak 1 and peak 2 can be different, but the observed PL spectra are always fit by the linear superposition of the two peaks. The position of peak 1 remains the same at 522 nm, whereas that of peak 2 can vary within 2-3 nm, (Figure S7). Also, we found that peak 2 is much more enhanced at the ASE-active spots, when compared with peak 2 from the ASE-inactive gray area. The observed dual PL feature is a well-known phenomenon in bulk halide perovskite crystals, composed of the band-edge PL (peak 1) and modified PL peak (peak 2) that is left after reabsorptions (see Figure S8 for different PL lifetimes for peak 1 and peak 2). We emphasize that the subtle variation of the PL was only measurable using the micro-PL setup.

Raman measurements were conducted at room temperature with a 632.8 nm laser and at 77 K with a 441.6 nm laser. (Figure 4b and S9). Both experiments showed that the two regions are indeed identical and all of the measured Raman peaks match with those previously reported for CsPbBr₃.⁵⁷

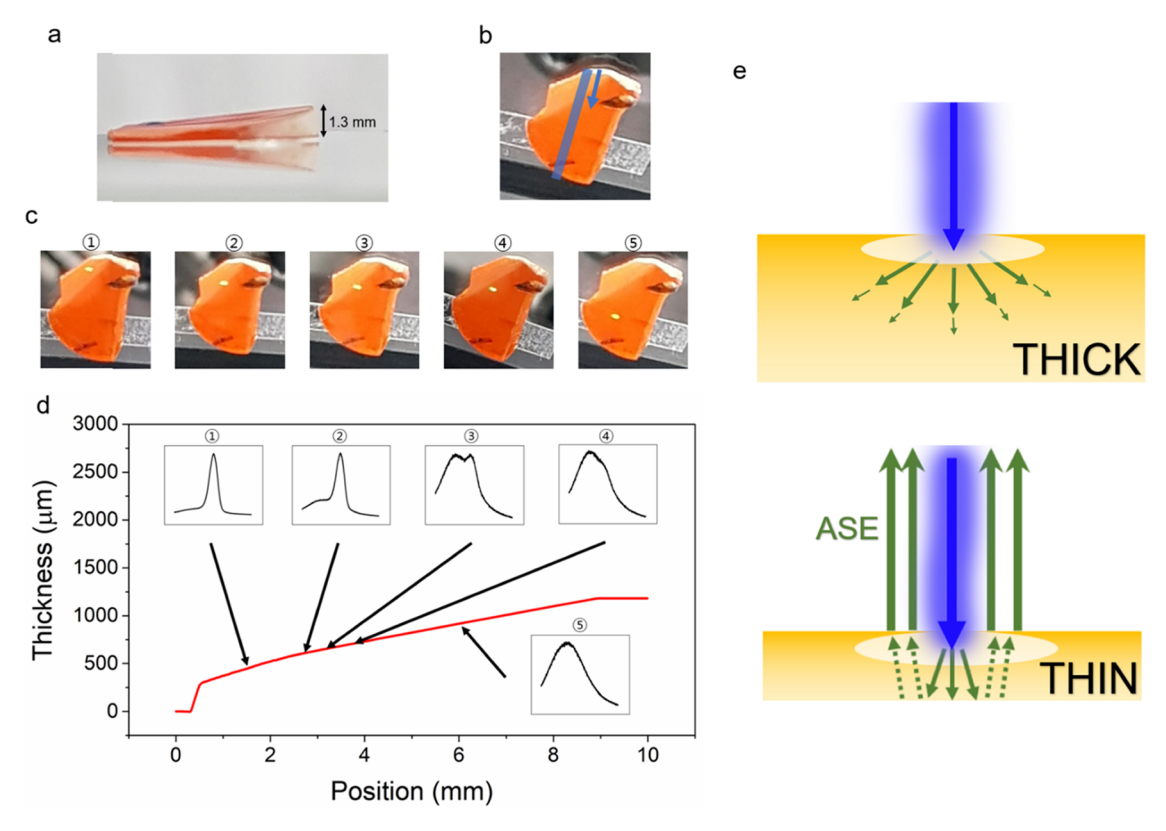


Figure 5. (a) Side view and (b) front view of the wedge-shaped CsPbBr₃ single crystal. The blue stripe and the arrow illustrate the area and the direction for the thickness scan. (c) Images of the sample under position-dependent laser excitation. (d) Thickness profile (red line) of the sample along the scan direction and the several PL spectra measured at the selected thicknesses under 1PA using λ = 520 nm and I = 300 MWcm⁻², clearly demonstrating the thickness dependence of ASE. Critical thickness for ASE at this excitation level was found to be 650~700 μm. The x and y axes of each PL spectrum in (d) represent the photon wavelength in the range of 520–560 nm and the PL counts (a.u), respectively. (e) Schematic for the PL mechanism for a thick sample (top) and a thin sample (bottom), where the latter supports ASE.

These results rule out any possibility of the orange inclusions that might correspond to off-stoichiometric phases of Cs₄PbBr₆ and CsPb₂Br₅, as well as the nonperovskite 1D polymorph of CsPbBr₃, thereby supporting that both regions consist entirely of the 3D CsPbBr₃.

Then, how do we understand this rather contradicting micro-PL and micro-Raman results, the former indicating the difference but the latter no difference between the two regions? Upon close and careful examination of the orange spots, we found that they always appear near local cracks and the abrupt edges of the crystal, indicating that the orange regions seem intact but are actually microcrystals that have separated from the bulk through the crack formation. This can alter the PL shape via different reabsorption effects depending on the actual size of the crystallites slightly cleaved from the bulk. To confirm our thesis, the bulky gray part was broken into powders and their optical properties were investigated. Interestingly, once it was prepared into powders, the crystallites immediately became orange in color (Figure S10) and showed exactly the same optical properties including ASE. Figure 4c shows the photographs of the bulk crystal and powders taken at several temperatures from 300 to 10 K. It is interesting to note that the powder looks brighter than the bulk counterpart at each temperature owing to suppressed reabsorption of the PL. We further confirmed that peak 2 is the modified PL via reabsorption by physically separating peak 1 and peak 2 with adjusting the slit width of our spectrometer (Figure S11). Based on this clear-cut result, we conclude that the apparent difference between the ASE-active and inactive ${\rm CsPbBr_3}$ does not arise from any extrinsic effect including defects or different stoichiometric perovskites but purely from the reabsorption effect of the PL depending on the physical size of the crystallites.

These small orange-colored crystallites exhibit seemingly different optical behaviors when embedded in a few mm thick bulk single crystals in terms of reabsorption and scattering. This is well demonstrated by the dark-field microscopy image (Figure 3d), where the embedded crystallites are distinctively bright compared with the bulk crystal. This means that the modified PL is more likely reflected at the edge and gets effectively scattered compared with the gray-colored bulk, where the majority of the PL is reabsorbed and lost. A clear contrast between the bulk and the crystallite can be directly observed under the microscope (Figure S12).

With a defocused pulsed laser beam, we were able to locate the embedded crystallites in real time (Supporting Information Video) that exhibit much brighter PL emission, thereby standing out from the rest of the crystal. Different spectral features of PL emission from the bulk and the small crystallite can be understood from the presence and the absence of reabsorption of the PL (peak 2 in Figure 4a). Secured School occur at the orange crystallites where the gain is ensured with minimal reabsorption of the PL. Slightly different positions of peak 2 arise most likely from the varying degrees of freedom in reabsorption within arbitrary geometry of the crystallites. An interesting but presumably key connection with ASE is that the wavelength for peak 2 coincides with the initial ASE wavelength before a red shift. Clearly, a high enough gain

in peak 2 is required for the emergence of ASE for population inversion. A wavelength-dependent micro-PL experiment further supports the close relation between peak 2 and ASE (Figure \$13).

To directly demonstrate the concept of thickness control for efficient ASE, we carried out the thickness scan using a wedgeshaped single crystal having a smooth surface without any crack and microcrystals on the surface (Figure 5a). The scan area and the direction are indicated by the blue stripe and arrow, respectively, in Figure 5b. Figure 5c shows the several excitation spots on the sample for the thickness scan under 1PA at $\lambda = 520$ nm and at I = 300 MWcm⁻². The corresponding PL spectra are shown in the inset of Figure 5d, which plots the thickness profile of the crystal with the arrows for the excitation positions. As predicted, ASE is much more prominent at the smallest thickness, where reabsorption of the PL is significantly suppressed. With increasing the thickness, ASE becomes weaker and disappears at 650-700 um, which is the critical thickness at this excitation condition. We emphasize that no position dependence in addition to thickness was found in this cleaved crystal. This result clearly shows that reabsorption can play a crucial role over optical gain in a thick CsPbBr3, but a bulk single crystal can lase through proper thickness control. Figure 5e schematically shows the impact of the sample thickness on ASE. In the thick sample, the PL is completely reabsorbed by traveling the macroscopic distance throughout the crystal. However, in the thin sample, the PL scattered inside the sample (dashed green arrow) triggers ASE in the population inversion region (white area). We also estimated the gain of the crystal by the variable stripe length method, which is detailed in Figure S14.

CONCLUSIONS

In conclusion, we have realized room-temperature ASE in CsPbBr₃ single crystals under one-photon excitation, clarified the origin of ASE, and explained its strong dependence on the excitation wavelength and the position as well. While the clean bulk single crystal appears dark gray under a confocal microscope, the ASE-active regions embedded as cleaved crystallites exhibit a bright orange color. We have demonstrated that these two seemingly different parts are indeed precisely identical through various optical characterizations. The difference in the apparent color and PL arises only from the different levels of reabsorption of the PL depending on the crystal size. Using a wedge-shaped sample, we have directly demonstrated that highly efficient ASE from a bulk CsPbBr₃ single crystal can be realized under typical 1PA at room temperature. For practical laser application, identifying an optimum thickness would be the key to achieving the most energy-effective lasing device.

ASSOCIATED CONTENT

XRD pattern, peak position and PL counts from PLE results, onset behavior of ASE, temperature-dependent PL spectrum of CsPbBr₃, power-dependent PL measurement at 80K, representative microscopy images of the sample under laser excitation, peak positions from micro-PL results, PL decay curves, low-temperature Raman measurement, microscopy image of the pow-

dered sample, PL results with slit-width adjustments, wavelength-dependent micro-PL results, and estimation of the gain (PDF)

Supporting Information Video (MP4)

AUTHOR INFORMATION

Corresponding Author

Joon I. Jang — Department of Physics, Sogang University, Seoul 04107, South Korea; orcid.org/0000-0002-1608-8321; Email: jjcoupling@sogang.ac.kr

Authors

Donggyu Kim – Department of Physics, Sogang University, Seoul 04107, South Korea; orcid.org/0000-0001-6905-9869

Hongsun Ryu – Department of Physics, Sogang University, Seoul 04107, South Korea

Soo Yeon Lim – Department of Physics, Sogang University, Seoul 04107, South Korea

Kyle M. McCall – Department of Chemistry, Northwestern University, Evanston, Illinois 60208, United States; Present Address: Laboratory of Inorganic Chemistry, Department of Chemistry and Applied Biosciences, ETH Zurich, 8093 Zurich, Switzerland

Jongwoo Park – Department of Physics and Energy Harvest Storage Research Center, University of Ulsan, Ulsan 44610, South Korea

Sungdo Kim — Department of Physics and Energy Harvest Storage Research Center, University of Ulsan, Ulsan 44610, South Korea; Occid.org/0000-0002-5472-9134

Tae Jung Kim – Department of Physics, Kyung Hee University, Seoul 02447, South Korea

Jeongyong Kim — Department of Energy Science, Sungkyunkwan University, Suwon 16419, South Korea; orcid.org/0000-0003-4679-0370

Yong Soo Kim – Department of Physics and Energy Harvest Storage Research Center, University of Ulsan, Ulsan 44610, South Korea

Mercouri G. Kanatzidis — Department of Chemistry, Northwestern University, Evanston, Illinois 60208, United States; © orcid.org/0000-0003-2037-4168

Hyeonsik Cheong – Department of Physics, Sogang University, Seoul 04107, South Korea; oorcid.org/0000-0002-2347-4044

Notes

The authors declare no competing financial interest.

ACKNOWLEDGMENTS

This work was supported by the Basic Science Research Programs (2019R1A2C3006189, 2017R1D1A1B03035539, 2020R1F1A1069646, and 2021R1A2C2013625) and the Priority Research Centers Program (2019R1A6A1A11053838) through the National Research Foundation of Korea (NRF), funded by the Korean government. Y.S.K. also thanks Technology Innovation Program (20009803), funded by the Ministry of Trade, Industry & Energy (MOITE, Korea). At the Northwestern University, this work was supported by the US Department of Energy, Office

of Science, Basic Energy Sciences, under grant no. SC0012541 (synthesis and structural characterization).

REFERENCES

- (1) Burschka, J.; Pellet, N.; Moon, S.; Humphry-Baker, R.; Gao, P.; Nazeeruddin, M. K.; Grätzel, M. Sequential deposition as a route to high-performance perovskite-sensitized solar cells. *Nature* **2013**, 499, 316.
- (2) Luo, J.; Im, J.; Mayer, M. T.; Schreier, M.; Nazeeruddin, M. K.; Park, N.; Tilley, S. D.; Fan, H. J.; Gratzel, M. Water photolysis at 12.3% efficiency via perovskite photovoltaics and Earth-abundant catalysts. *Science* **2014**, *345*, 1593.
- (3) Yang, W. S.; Noh, J. H.; Jeon, N. J.; Kim, Y. C.; Ryu, S.; Seo, J.; Seok, S. I. High-performance photovoltaic perovskite layers fabricated through intramolecular exchange. *Science* **2015**, 348, 1234.
- (4) Śwarnkar, A.; Marshall, A. R.; Sanehira, E. M.; Chernomordik, B. D.; Moore, D. T.; Christians, J. A.; Chakrabarti, T.; Luther, J. M. Quantum dot-induced phase stabilization of α -CsPbI₃ perovskite for high-efficiency photovoltaics. *Science* **2016**, 354, 92.
- (5) Jung, E. H.; Jeon, N. J.; Park, E. Y.; Moon, C. S.; Shin, T. J.; Yang, T.; Noh, J. H.; Seo, J. Efficient, stable and scalable perovskite solar cells using poly(3-hexylthiophene). *Nature* **2019**, *567*, 511.
- (6) Lin, K.; Xing, J.; Quan, L. N.; de Arquer, F. P. G.; Gong, X.; Lu, J.; Xie, L.; Zhao, W.; Zhang, D.; Yan, C.; Li, W.; Liu, X.; Lu, Y.; Kirman, J.; Sargent, E. H.; Xiong, Q.; Wei, Z. Perovskite light-emitting diodes with external quantum efficiency exceeding 20 per cent. *Nature* 2018, 562, 245.
- (7) Tan, Z.; Moghaddam, R. S.; Lai, M. L.; Docampo, P.; Higler, R.; Deschler, F.; Price, M.; Sadhanala, A.; Pazos, L. M.; Credgington, D.; Hanusch, F.; Bein, T.; Snaith, H. J.; Friend, R. H. Bright light-emitting diodes based on organometal halide perovskite. *Nat. Nanotechnol.* **2014**, *9*, 687.
- (8) Wang, N.; Cheng, L.; Ge, R.; Zhang, S.; Miao, Y.; Zou, W.; Yi, C.; Sun, Y.; Cao, Y.; Yang, R.; Wei, Y.; Guo, Q.; Ke, Y.; Yu, M.; Jin, Y.; Liu, Y.; Ding, Q.; Di, D.; Yang, L.; Xing, G.; Tian, H.; Jin, C.; Gao, F.; Friend, R. H.; Wang, J.; Huang, W. Perovskite light-emitting diodes based on solution-processed self-organized multiple quantum wells. *Nat. Photonics* **2016**, *10*, 699.
- (9) Dong, Q.; Fang, Y.; Shao, Y.; Mulligan, P.; Qiu, J.; Cao, L.; Huang, J. Electron-hole diffusion lengths> 175 μ m in solution-grown CH3NH3PbI3 single crystals. *Science* **2015**, *347*, 967.
- (10) Shi, D.; Adinolfi, V.; Comin, R.; Yuan, M.; Alarousu, E.; Buin, A.; Chen, Y.; Hoogland, S.; Rothenberger, A.; Katsiev, K.; Losovyj, Y.; Zhang, X.; Dowben, P. A.; Mohammed, O. F.; Sargent, E. H.; Bakr, O. M. Solar cells. Low trap-state density and long carrier diffusion in organolead trihalide perovskite single crystals. *Science* **2015**, 347, 519.
- (11) Stranks, S. D.; Eperon, G. E.; Grancini, G.; Menelaou, C.; Alcocer, M. J. P.; Leijtens, T.; Herz, L. M.; Petrozza, A.; Snaith, H. J. Electron-Hole Diffusion Lengths Exceeding 1 Micrometer in an Organometal Trihalide Perovskite Absorber. *Science* **2013**, 342, 341.
- (12) Xing, G.; Mathews, N.; Sun, S.; Lim, S. S.; Lam, Y. M.; Gratzel, M.; Mhaisalkar, S.; Sum, T. C. Long-Range Balanced Electron- and Hole-Transport Lengths in Organic-Inorganic CH₃NH₃PbI₃. *Science* **2013**, 342, 344.
- (13) Liu, P.; He, X.; Ren, J.; Liao, Q.; Yao, J.; Fu, H. Organic—Inorganic Hybrid Perovskite Nanowire Laser Arrays. ACS Nano 2017, 11. 5766.
- (14) Chen, S.; Roh, K.; Lee, J.; Chong, W. K.; Lu, Y.; Mathews, N.; Sum, T. C.; Nurmikko, A. A Photonic Crystal Laser from Solution Based Organo-Lead Iodide Perovskite Thin Films. *ACS Nano* **2016**, *10*, 3959.
- (15) Eaton, S. W.; Lai, M.; Gibson, N. A.; Wong, A. B.; Dou, L.; Ma, J.; Wang, L.-W.; Leone, S. R.; Yang, P. Lasing in robust cesium lead halide perovskite nanowires. *Proc. Natl. Acad. Sci. U.S.A.* **2016**, *113*, 1993.
- (16) Park, K.; Lee, J. W.; Kim, J. D.; Han, N. S.; Jang, D. M.; Jeong, S.; Park, J.; Song, J. K. Light–Matter Interactions in Cesium Lead Halide Perovskite Nanowire Lasers. *J. Phys. Chem. Lett.* **2016**, *7*, 3703.

- (17) Wang, Y.; Li, X.; Zhao, X.; Xiao, L.; Zeng, H.; Sun, H. Nonlinear Absorption and Low-Threshold Multiphoton Pumped Stimulated Emission from All-Inorganic Perovskite Nanocrystals. *Nano Lett.* **2016**, *16*, 448.
- (18) Protesescu, L.; Yakunin, S.; Bodnarchuk, M. I.; Krieg, F.; Caputo, R.; Hendon, C. H.; Yang, R. X.; Walsh, A.; Kovalenko, M. V. Nanocrystals of Cesium Lead Halide Perovskites (CsPbX₃, X = Cl, Br, and I): Novel Optoelectronic Materials Showing Bright Emission with Wide Color Gamut. *Nano Lett.* **2015**, *15*, 3692.
- (19) Yakunin, S.; Protesescu, L.; Krieg, F.; Bodnarchuk, M. I.; Nedelcu, G.; Humer, M.; De Luca, G.; Fiebig, M.; Heiss, W.; Kovalenko, M. V. Low-threshold amplified spontaneous emission and lasing from colloidal nanocrystals of caesium lead halide perovskites. *Nat. Commun.* **2015**, *6*, No. 8056.
- (20) Li, J.; Si, J.; Gan, L.; Liu, Y.; Ye, Z.; He, H. Simple Approach to Improving the Amplified Spontaneous Emission Properties of Perovskite Films. ACS Appl. Mater. Interfaces 2016, 8, 32978.
- (21) Pourdavoud, N.; Haeger, T.; Mayer, A.; Cegielski, P. J.; Giesecke, A. L.; Heiderhoff, R.; Olthof, S.; Zaefferer, S.; Shutsko, I.; Henkel, A.; Becker-Koch, D.; Stein, M.; Cehovski, M.; Charfi, O.; Johannes, H.; Rogalla, D.; Lemme, M. C.; Koch, M.; Vaynzof, Y.; Meerholz, K.; Kowalsky, W.; Scheer, H.; Görrn, P.; Riedl, T. Room-Temperature Stimulated Emission and Lasing in Recrystallized Cesium Lead Bromide Perovskite Thin Films. *Adv. Mater.* **2019**, *31*, No. 1903717.
- (22) Guo, P.; Hossain, M. K.; Shen, X.; Sun, H.; Yang, W.; Liu, C.; Ho, C. Y.; Kwok, C. K.; Tsang, S.; Luo, Y.; Ho, J. C.; Yu, K. M. Room-Temperature Red-Green-Blue Whispering-Gallery Mode Lasing and White-Light Emission from Cesium Lead Halide Perovskite (CsPbX₃, X = Cl, Br, I) Microstructures. *Adv. Opt. Mater.* **2018**, *6*, No. 1700993.
- (23) Dey, A.; Rathod, P.; Kabra, D. Role of Localized States in Photoluminescence Dynamics of High Optical Gain CsPbBr₃ Nanocrystals. *Adv. Opt. Mater.* **2018**, *6*, No. 1800109.
- (24) Papagiorgis, P.; Manoli, A.; Protesescu, L.; Achilleos, C.; Violaris, M.; Nicolaides, K.; Trypiniotis, T.; Bodnarchuk, M. I.; Kovalenko, M. V.; Othonos, A.; Itskos, G. Efficient Optical Amplification in the Nanosecond Regime from Formamidinium Lead Iodide Nanocrystals. ACS Photonics 2018, 5, 907.
- (25) Veldhuis, S. A.; Tay, Y. K. E.; Bruno, A.; Dintakurti, S. S. H.; Bhaumik, S.; Muduli, S. K.; Li, M.; Mathews, N.; Sum, T. C.; Mhaisalkar, S. G. Benzyl Alcohol-Treated CH₃NH₃PbBr₃ Nanocrystals Exhibiting High Luminescence, Stability, and Ultralow Amplified Spontaneous Emission Thresholds. *Nano Lett.* **2017**, *17*, 7424.
- (26) Nagamine, G.; Rocha, J. O.; Bonato, L. G.; Nogueira, A. F.; Zaharieva, Z.; Watt, A. A. R.; de Brito Cruz, C. H.; Padilha, L. A. Two-Photon Absorption and Two-Photon-Induced Gain in Perovskite Quantum Dots. *J. Phys. Chem. Lett.* **2018**, *9*, 3478.
- (27) Huang, C.; Zou, C.; Mao, C.; Corp, K. L.; Yao, Y.; Lee, Y.; Schlenker, C. W.; Jen, A. K. Y.; Lin, L. Y. CsPbBr 3 Perovskite Quantum Dot Vertical Cavity Lasers with Low Threshold and High Stability. ACS Photonics 2017, 4, 2281.
- (28) Fu, Y.; Zhu, H.; Stoumpos, C. C.; Ding, Q.; Wang, J.; Kanatzidis, M. G.; Zhu, X.; Jin, S. Broad Wavelength Tunable Robust Lasing from Single-Crystal Nanowires of Cesium Lead Halide Perovskites (CsPbX₃, X = Cl, Br, I). ACS Nano **2016**, 10, 7963.
- (29) Deschler, F.; Price, M.; Pathak, S.; Klintberg, L. E.; Jarausch, D.; Higler, R.; Hüttner, S.; Leijtens, T.; Stranks, S. D.; Snaith, H. J.; Atatüre, M.; Phillips, R. T.; Friend, R. H. High Photoluminescence Efficiency and Optically Pumped Lasing in Solution-Processed Mixed Halide Perovskite Semiconductors. *J. Phys. Chem. Lett.* **2014**, *5*, 1421.
- (30) Harwell, J. R.; Whitworth, G. L.; Turnbull, G. A.; Samuel, I. D. W. Green Perovskite Distributed Feedback Lasers. *Sci. Rep.* **2017**, *7*, No. 11727.
- (31) Whitworth, G. L.; Harwell, J. R.; Miller, D. N.; Hedley, G. J.; Zhang, W.; Snaith, H. J.; Turnbull, G. A.; Samuel, I. D. W. Nanoimprinted distributed feedback lasers of solution processed hybrid perovskites. *Opt. Express* **2016**, *24*, 23677.

- (32) Kurahashi, N.; Nguyen, V.; Sasaki, F.; Yanagi, H. Whispering gallery mode lasing in lead halide perovskite crystals grown in microcapillary. *Appl. Phys. Lett.* **2018**, *113*, No. 011107.
- (33) Zhang, Q.; Ha, S. T.; Liu, X.; Sum, T. C.; Xiong, Q. Room-Temperature Near-Infrared High-Q Perovskite Whispering-Gallery Planar Nanolasers. *Nano Lett.* **2014**, *14*, 5995.
- (34) Murzin, A. O.; Stroganov, B. V.; Günnemann, C.; Hammouda, S. B.; Shurukhina, A. V.; Lozhkin, M. S.; Emeline, A. V.; Kapitonov, Y. V. Amplified Spontaneous Emission and Random Lasing in MAPbBr₃ Halide Perovskite Single Crystals. *Adv. Opt. Mater.* **2020**, 8, No. 2000690.
- (35) Zhao, C.; Tian, W.; Liu, J.; Sun, Q.; Luo, J.; Yuan, H.; Gai, B.; Tang, J.; Guo, J.; Jin, S. Stable Two-Photon Pumped Amplified Spontaneous Emission from Millimeter-Sized CsPbBr₃ Single Crystals. J. Phys. Chem. Lett. **2019**, 10, 2357.
- (36) Li, X.; Wang, K.; Chen, M.; Wang, S.; Fan, Y.; Liang, T.; Song, Q.; Xing, G.; Tang, Z. Stable Whispering Gallery Mode Lasing from Solution-Processed Formamidinium Lead Bromide Perovskite Microdisks. *Adv. Opt. Mater.* **2020**, *8*, No. 2000030.
- (37) Liu, Y.; Wang, J.; Zhang, L.; Liu, W.; Wu, C.; Liu, C.; Wu, Z.; Xiao, L.; Chen, Z.; Wang, S. Exciton and bi-exciton mechanisms in amplified spontaneous emission from CsPbBr₃ perovskite thin films. *Opt. Express* **2019**, 27, 29124.
- (38) Navarro-Arenas, J.; Suárez, I.; Chirvony, V. S.; Gualdrón-Reyes, A. F.; Mora-Seró, I.; Martínez-Pastor, J. Single-Exciton Amplified Spontaneous Emission in Thin Films of CsPbX₃ (X = Br, I) Perovskite Nanocrystals. *J. Phys. Chem. Lett.* **2019**, *10*, 6389.
- (39) Suárez, I.; Juárez-Pérez, E. J.; Chirvony, V. S.; Mora-Seró, I.; Martínez-Pastor, J. P. Mechanisms of Spontaneous and Amplified Spontaneous Emission in CH₃NH₃PbI₃ Perovskite Thin Films Integrated in an Optical Waveguide. *Phys. Rev. Appl.* **2020**, *13*, No. 064071.
- (40) Bao, W.; Liu, X.; Xue, F.; Zheng, F.; Tao, R.; Wang, S.; Xia, Y.; Zhao, M.; Kim, J.; Yang, S.; Li, Q.; Wang, Y.; Wang, Y.; Wang, L.; MacDonald, A. H.; Zhang, X. Observation of Rydberg exciton polaritons and their condensate in a perovskite cavity. *Proc. Natl. Acad. Sci. U.S.A.* **2019**, *116*, 20274.
- (41) Su, R.; Diederichs, C.; Wang, J.; Liew, T. C. H.; Zhao, J.; Liu, S.; Xu, W.; Chen, Z.; Xiong, Q. Room-Temperature Polariton Lasing in All-Inorganic Perovskite Nanoplatelets. *Nano Lett.* **2017**, *17*, 3982.
- (42) Shang, Q.; Li, M.; Zhao, L.; Chen, D.; Zhang, S.; Chen, S.; Gao, P.; Shen, C.; Xing, J.; Xing, G.; Shen, B.; Liu, X.; Zhang, Q. Role of the Exciton-Polariton in a Continuous-Wave Optically Pumped CsPbBr, Perovskite Laser. *Nano Lett.* **2020**, *20*, 6636.
- (43) Wang, Y.; Zhi, M.; Chang, Y.; Zhang, J.; Chan, Y. Stable, Ultralow Threshold Amplified Spontaneous Emission from CsPbBr₃ Nanoparticles Exhibiting Trion Gain. *Nano Lett.* **2018**, *18*, 4976.
- (44) Booker, E. P.; Price, M. B.; Budden, P. J.; Abolins, H.; del Valle-Inclan Redondo, Y.; Eyre, L.; Nasrallah, I.; Phillips, R. T.; Friend, R. H.; Deschler, F.; Greenham, N. C. Vertical Cavity Biexciton Lasing in 2D Dodecylammonium Lead Iodide Perovskites. *Adv. Opt. Mater.* **2018**, *6*, No. 1800616.
- (45) Zhao, W.; Qin, Z.; Zhang, C.; Wang, G.; Huang, X.; Li, B.; Dai, X.; Xiao, M. Optical Gain from Biexcitons in CsPbBr₃ Nanocrystals Revealed by Two-dimensional Electronic Spectroscopy. *J. Phys. Chem. Lett.* **2019**, *10*, 1251.
- (46) Stoumpos, C. C.; Malliakas, C. D.; Peters, J. A.; Liu, Z.; Sebastian, M.; Im, J.; Chasapis, T. C.; Wibowo, A. C.; Chung, D. Y.; Freeman, A. J.; Wessels, B. W.; Kanatzidis, M. G. Crystal Growth of the Perovskite Semiconductor CsPbBr₃: A New Material for High-Energy Radiation Detection. *Cryst. Growth Des.* **2013**, *13*, 2722.
- (47) Wenger, B.; Nayak, P. K.; Wen, X.; Kesava, S. V.; Noel, N. K.; Snaith, H. J. Consolidation of the optoelectronic properties of CH₃NH₃PbBr₃ perovskite single crystals. *Nat. Commun.* **2017**, *8*, No. 590.
- (48) Wu, B.; Yuan, H.; Xu, Q.; Steele, J. A.; Giovanni, D.; Puech, P.; Fu, J.; Ng, Y. F.; Jamaludin, N. F.; Solanki, A.; Mhaisalkar, S.; Mathews, N.; Roeffaers, M. B. J.; Grätzel, M.; Hofkens, J.; Sum, T. C.

- Indirect tail states formation by thermal-induced polar fluctuations in halide perovskites. *Nat. Commun.* **2019**, *10*, No. 484.
- (49) Ryu, H.; Park, D. Y.; McCall, K.; Byun, H. R.; Lee, Y.; Kim, T. J.; Jeong, M. S.; Kim, J.; Kanatzidis, M. G.; Jang, J. I. Static Rashba Effect by Surface Reconstruction and Photon Recycling in the Dynamic Indirect Gap of APbBr₃ (A = Cs, CH₃NH₃) Single Crystals. *J. Am. Chem. Soc.* **2020**, 142, 21059.
- (50) Price, M. B.; Butkus, J.; Jellicoe, T. C.; Sadhanala, A.; Briane, A.; Halpert, J. E.; Broch, K.; Hodgkiss, J. M.; Friend, R. H.; Deschler, F. Hot-carrier cooling and photoinduced refractive index changes in organic—inorganic lead halide perovskites. *Nat. Commun.* **2015**, *6*, No. 8420.
- (51) Ryu, H.; Byun, H. R.; McCall, K. M.; Park, D. Y.; Kim, T. J.; Jeong, M. S.; Kanatzidis, M. G.; Jang, J. I. Role of the A-site cation in low-temperature optical behaviors of APbBr₃ (A = Cs, CH₃NH₃). *J. Am. Chem. Soc.* **2021**, *143*, 2340.
- (52) Shen, J.; Zhang, X.; Das, S.; Kioupakis, E.; Van de Walle, Chris G. Unexpectedly Strong Auger Recombination in Halide Perovskites. *Adv. Energy Mater.* **2018**, *8*, No. 1801027.
- (53) Jang, J. I.; Wolfe, J. P. Auger recombination and biexcitons in Cu2O: A case for dark excitonic matter. *Phys. Rev. B* **2006**, *74*, No. 045211.
- (54) Lee, H. C. Theoretical Study of Auger Recombination of Excitons in Monolayer Transition-metal Dichalcogenides. *J. Korean Phys. Soc.* **2018**, *73*, 1735–1743.
- (55) Schlaus, A. P.; Spencer, M. S.; Miyata, K.; Liu, F.; Wang, X.; Datta, I.; Lipson, M.; Pan, A.; Zhu, X. Y. How lasing happens in CsPbBr3 perovskite nanowires. *Nat. Commun.* **2019**, *10*, No. 265.
- (56) Nagai, M.; Kuwata-Gonokami, M. Electron—hole liquid formation by exciton and biexciton resonant excitation in CuCl. *J. Lumin.* **2002**, *100*, 233–242.
- (57) Cha, J.; Han, J. H.; Yin, W.; Park, C.; Park, Y.; Ahn, T. K.; Cho, J. H.; Jung, D. Photoresponse of CsPbBr₃ and Cs₄PbBr₆ Perovskite Single Crystals. *J. Phys. Chem. Lett.* **2017**, *8*, 565.
- (58) Aebli, M.; Benin, B. M.; McCall, K. M.; Morad, V.; Thöny, D.; Grützmacher, H.; Kovalenko, M. V. White CsPbBr₃: Characterizing the One-Dimensional Cesium Lead Bromide Polymorph. *Helv. Chim. Acta* **2020**, *103*, No. e2000080.
- (59) Hong, D.; Li, J.; Wan, S.; Scheblykin, I. G.; Tian, Y. Red-Shifted Photoluminescence from Crystal Edges Due to Carrier Redistribution and Reabsorption in Lead Triiodide Perovskites. *J. Phys. Chem. C* **2019**, *123*, 12521.